

Crystal-to-crystal phase transformation of Fe₃O₄ magnetite under uniaxial compression

Masaaki MISAWA¹, Kohei SHIMAMURA² and Fuyuki SHIMOJO¹

¹*Department of Physics, Kumamoto University, Kumamoto 860-8555*

²*Graduate School of System Informatics, Kobe University, Kobe 657-8501*

(Received May 31, 2017)

Structural properties of magnetite under a uniaxial compression have been investigated based on first-principles molecular dynamics simulations. A significant structural transformation was observed when the uniaxial compression of 50 GPa was applied in magnetite along the [110] direction. This crystal-to-crystal transformation was irreversible and obtained structures were clearly distinct from the hydrostatic high-pressure phases already reported. It is expected that the obtained crystal phases exhibit different magnetic or electronic properties from the other crystalline phases and may be helpful to understand the complex phase transformation mechanisms of magnetite such as the Verwey transition.

§1. Introduction

Iron oxides attract a lot of attention as a next-generation spintronics device, photo catalyst, ceramics or other many functional materials because of its unique electronic properties and abundance in Earth's crust. There is a lot of compositions (e.g. FeO, Fe₂O₃ or Fe₃O₄) and crystal structure (e.g. corundum, bcc or defective spinel structures in Fe₂O₃) in iron oxides, and those various phases exhibit quite different structural and electronic properties.¹⁾

Magnetite (Fe₃O₄) is well known as one of important compounds among iron oxides because it exhibits spontaneous magnetization under ambient conditions. The spontaneous magnetization arises from the existence of two types of Fe atoms in the crystal structure, the tetrahedral centered Fe (Fe_A) and octahedral centered Fe (Fe_B) atoms.²⁾ The different and opposite atomic magnetic moments of Fe_A and Fe_B cause ferri-magnetism. Because of this property, magnetite has been well studied and used as a magnetic material for a long time.

Magnetite exhibits some structural transformations under various conditions. The most famous one is the metal-insulator transition under low temperature (< 120 K), named Verwey transition.³⁾ During this transition, the stable half-metallic cubic structure under ambient conditions transformed into monoclinic structure accompanied by a sudden sharp decrease in electric conductivity below 120 K. This transition mechanism has not been completely explained yet even though various studies have been conducted.⁴⁻⁶⁾

A few years ago, it was reported that the critical temperature of the Verwey transition becomes lower when single-crystalline magnetite was compressed along the [110] direction.⁶⁾ This result indicates that the structural and electronic properties of magnetite along the [110] direction play a dominant role in the Verwey transition. It is

considered that the investigation of the structural and electronic properties in magnetite under uniaxial high-pressure is helpful to understand the mechanism of the Verwey transition. For this purpose, we have investigated effects of the uniaxial high-pressure on the structural and electronic properties of magnetite. In this paper, we report the structural changes in magnetite under uniaxial compression of 50 GPa along the [110] direction.

§2. Computational Method

We calculated the electronic states based on the projector augmented-wave method within the framework of density functional theory.⁷⁾ The generalized gradient approximation was used for the exchange correlation energy.⁸⁾ To consider the on-site Coulomb interaction of the localized *d*-electrons, the DFT+*U* method was employed with $U_{\text{eff}} = 3.6$ eV.⁹⁾ The plane-wave cutoff energies were 20 and 300 Ry. for the electronic wave functions and charge density, respectively. The Γ point was used for Brillouin zone sampling. Projector functions were generated for the 3*d*, 4*s* and 4*p* states of Fe and for the 2*s* and 2*p* states of O. Using the Nosé-Hoover thermostat technique.¹⁰⁾ The equations of motion were solved via an explicit reversible integrator.¹¹⁾ All of the simulations were performed at room temperature (300 K) with the time step of 1.2 fs.

The stable phase of single-crystalline magnetite under ambient condition is cubic *Fd-3m* phase. We employed $2 \times 2 \times 2$ of pseudo-tetragonal crystal structure as the initial configuration of the simulation cell that includes 224 atoms (32 Fe_3O_4). The periodic boundary condition was taken into account in all direction. As mentioned in the introduction, it is well known that the cubic phase of magnetite exhibits ferri-magnetism due to the local magnetic moments of Fe atoms on two crystal sites A and B. The atomic magnetic moment of Fe atoms on the A site (Fe_A) is antiparallel to those on the B site (Fe_B). As the initial local magnetic moment, we employed -4.0 and $3.9 \mu_B/\text{atom}$ for the Fe_A and Fe_B atoms, respectively.¹²⁾ A uniaxial compression was generated by using the omni-directional multi-scale shock technique (OD-MSST) with a shock speed $v_s = 0$.¹³⁾

§2. Results and discussions

3.1. MD simulations

First, we performed MD simulation at room temperature (300 K) and ambient pressure (0 GPa) to verify the stability of the crystal structure of magnetite under ambient condition. The total simulation time is 0.75 ps. As a result of the simulation, we obtained the cubic phase with the lattice constant $a = 8.58 \text{ \AA}$ (Fig. 1(a)), which is a good agreement with a previous study.¹⁴⁾ Next, a uniaxial compression of 50 GPa was applied along the [110] direction of the crystal axis during 1.21 ps. In this process, a significant structural transformation from cubic to uniaxial strained (US) phase was observed (Fig. 1(b)). After that, the pressure was released and a MD simulation at ambient pressure was performed during 0.46 ps in order to obtain a relaxed US (RUS)

phase (Fig. 1(c)).

During the structural transformation process, coordination geometries around Fe atoms have changed. It is well known that the Fe_A and Fe_B atoms form FeO_4 tetrahedral units (*Tet* units, Fig. 1(d)) and FeO_6 octahedral units (*Oct* units, Fig. 1(e)) in the ambient cubic phase, respectively. The composition ratio is $\text{Tet} : \text{Oct} = 1 : 2$. In the US phase, half of the Fe_B (Fe_{B1}) atoms kept the *Oct* geometry throughout the simulation, while the Fe_A and the other half of Fe_B (Fe_{B2}) atoms changed into FeO_6 trigonal prismatic units (*Trp* units, Fig. 1(f)) and FeO_7 square face mono-capped trigonal prismatic units (*sfm-Trp* units, Fig. 1(g)) under the uniaxial high-pressure, respectively. In the US phase, the composition ratio of units was $\text{Oct} : \text{Trp} : \text{sfm-Trp} = 1 : 1 : 1$. In the RUS phase, only the Fe_{B1} atoms transformed into the *Trp* units. The Fe_A and Fe_{B2} atoms kept their coordination geometries in the US phase. In the RUS phase, the composition ratio was $\text{Oct} : \text{Trp} = 1 : 2$.

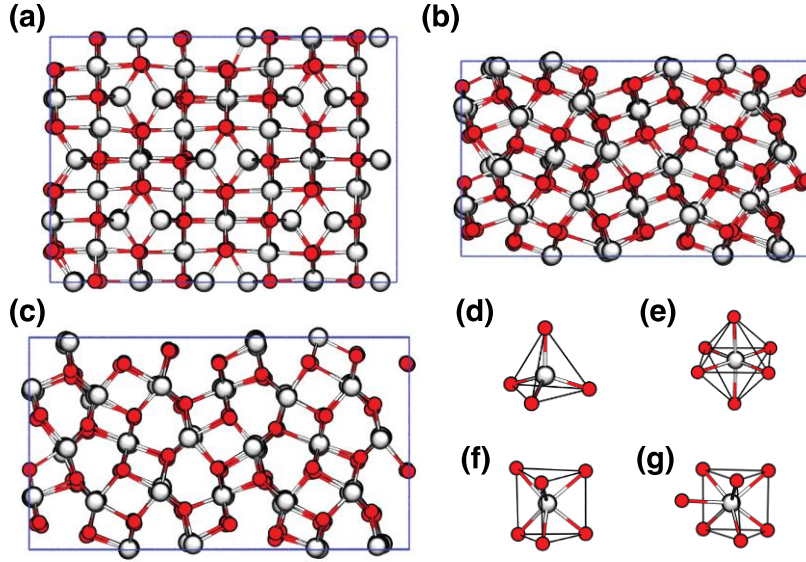


Fig. 1. (a-c) Snapshots of the cubic (a), US (b) and RUS (c) phase. The large white and small red spheres indicate Fe and O atoms, respectively. The blue lines illustrate the boundary of the simulation cell. The uniaxial compression is applied in downward of these pictures. (d-g) Coordination geometries of FeO_4 *Tet* (d), FeO_6 *Oct* (e), FeO_6 *Trp* (f) and FeO_7 *sfm-Trp* unit (g).

3.2. Structural analysis

Next the radial distribution functions $g(r)$ are calculated. Figure 2 shows the partial radial distribution functions for $\text{Fe}_A\text{-O}$, $\text{Fe}_{B1}\text{-O}$ and $\text{Fe}_{B2}\text{-O}$. From these radial distribution functions, we determined that the nearest neighbor distance between Fe and O atoms is 2.55 \AA (gray dashed dotted line). In the cubic phase, the radial

distribution functions of $\text{Fe}_{\text{B}1}\text{-O}$ and $\text{Fe}_{\text{B}2}\text{-O}$ are completely equal because the $\text{Fe}_{\text{B}1}$ and $\text{Fe}_{\text{B}2}$ atoms locate on same symmetric site in the cubic phase (top panel of Fig. 2). Under the uniaxial high-pressure, the first peak position of the radial distribution functions for $\text{Fe}_{\text{A}}\text{-O}$ and $\text{Fe}_{\text{B}2}\text{-O}$ shifted in the long distance side and second peaks around $r = 3.5$ broadened (middle panel of Fig. 2). This change corresponds to the uniaxial strain effect. After released the pressure (bottom panel of Fig. 2), the radial distribution functions of $\text{Fe}_{\text{A}}\text{-O}$ and $\text{Fe}_{\text{B}2}\text{-O}$ show good agreement above $r = 2.6$ Å because both the Fe_{A} and $\text{Fe}_{\text{B}2}$ atoms form *Trp* unit in RUS phase. However, the first peak positions of $\text{Fe}_{\text{A}}\text{-O}$ and $\text{Fe}_{\text{B}2}\text{-O}$ show disagreement. This result indicates that either the $\text{Fe}_{\text{B}1}$ or $\text{Fe}_{\text{B}2}$ atoms are forming distorted *Trp* units and those atoms may locate on different symmetric sites.

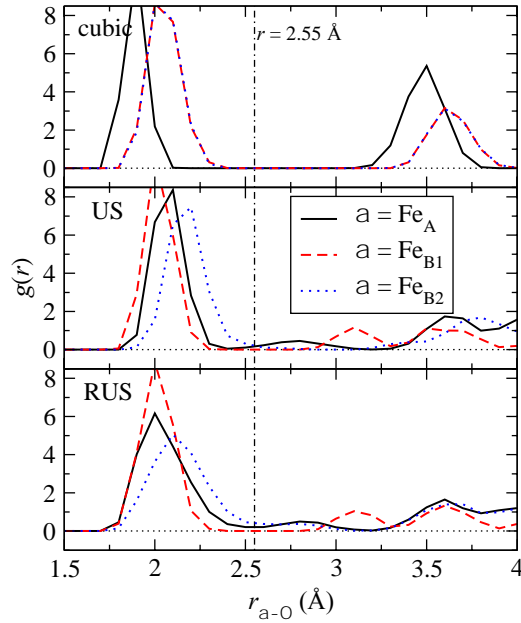


Fig. 2. Partial Radial distribution functions of the cubic (top), US (middle) and RUS (bottom) phases. The black solid, red dashed and blue dotted curves shows the radial distribution functions around the Fe_{A} , $\text{Fe}_{\text{B}1}$ and $\text{Fe}_{\text{B}2}$ atoms, respectively. The gray dashed dotted line indicates the nearest neighbor distance between Fe and O atoms estimated from the radial distribution functions.

The bond angle distribution functions $p(\theta)$ for the $\text{O}-\alpha\text{-O}$ ($\alpha = \text{Fe}_{\text{A}}$, $\text{Fe}_{\text{B}1}$ and $\text{Fe}_{\text{B}2}$) were calculated with the bond cutoff distance of 2.55 Å in order to make certain of shape of the coordination geometries (Fig. 3). In the cubic phase, we can see the peak positions that correspond to the *Tet* and *Oct* units clearly. The peak positions of $\text{O}-\text{Fe}_{\text{A}}\text{-O}$ angle in the US and RUS phases show characteristic shape of the *Trp* units. On the other hand, the distributions of the $\text{O}-\text{Fe}_{\text{B}1}\text{-O}$ and $\text{O}-\text{Fe}_{\text{B}2}\text{-O}$ angles were

broadened in the US and RUS phases. This result shows that the *Oct*, *Trp* and *sfm-Trp* units formed by $\text{Fe}_{\text{B}1}$ and $\text{Fe}_{\text{B}2}$ were distorted. This result well explains the difference in the radial distribution functions of $\text{Fe}_{\text{A}}\text{-O}$ and $\text{Fe}_{\text{B}2}\text{-O}$ at the RUS phase.

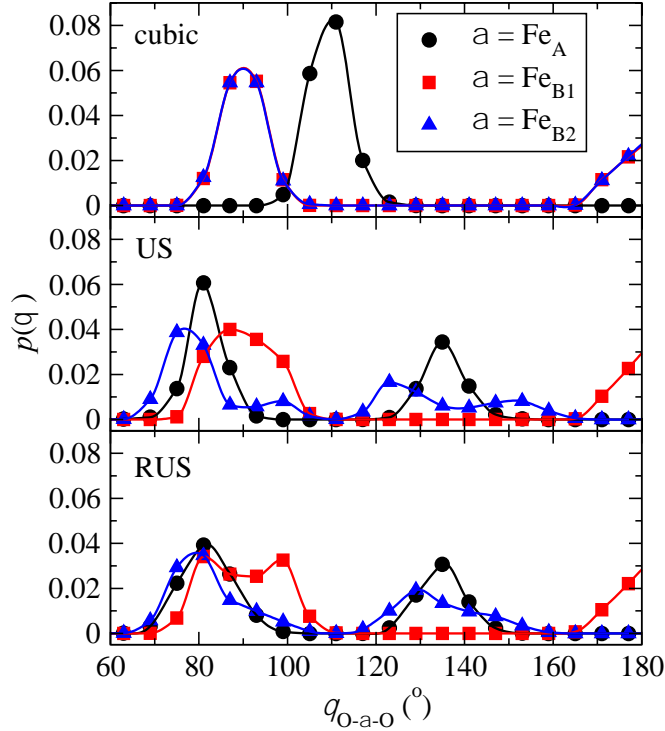


Fig. 3. Bond angle distribution function of the $\text{O-Fe}_{\text{A}}\text{-O}$ (black circle), $\text{O-Fe}_{\text{B}1}\text{-O}$ (red square) and $\text{O-Fe}_{\text{B}2}\text{-O}$ (blue triangle) in the cubic (top), US (middle) and RUS (bottom) phase.

Now we should mention about the hydrostatic high-pressure phase of magnetite. It has been reported that the two types of high-pressure phases, a *Pbcm* phase (at 29.7 GPa) and *Bbmm* phase (at 65.1 GPa).^{12,15,16} Those high-pressure phases consist of FeO_6 *Oct* and *Trp* units. In order to demonstrate that our uniaxial high-pressure phase is clearly different from the previously reported hydrostatic high-pressure phases, the total radial distribution functions of RUS, *Pbcm* and *Bbmm* phases are calculated (Fig. 4). The radial distribution functions of RUS phase was calculated by optimized structure of RUS phase at ambient pressure and those of *Pbcm* and *Bbmm* phases were obtained using structural parameters determined by experimental structural analysis.^{15,16} This figure shows the *Pbcm* and RUS structures have distinct difference in the number of peaks. We can see the difference between the *Bbmm* and RUS phases in sharp peak around $r = 3.0 \text{ \AA}$. It is considered that the specific peak of RUS phase corresponds to the anisotropic Fe-Fe correlation arisen from uniaxial strain.

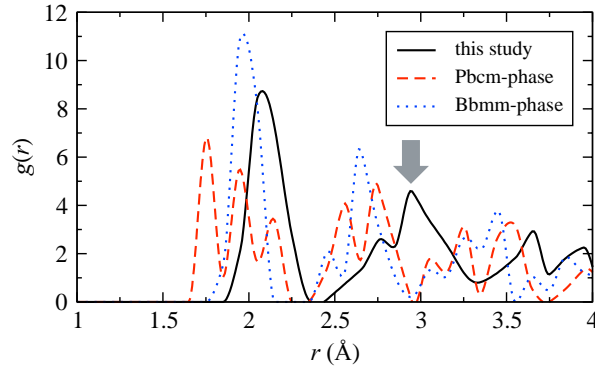


Fig. 4. Total radial distribution functions of optimized uniaxial high-pressure (black solid), the *Pbcm* (red dashed) and the *Bbmm* (blue dotted) phases.

Finally, we calculated time evolution of the average coordination numbers N_α ($\alpha = \text{Fe}_A, \text{Fe}_{B1}$ and Fe_{B2}) with the bond cutoff distance of 2.55 Å (Fig. 5). This figure confirmed that the FeO_7 *sfm-Trp* units exist certainly in US phase and only Fe_{B2} atoms formed this coordination geometry. Furthermore, it is found that the *Tet-to-Trp* and *Oct-to-sfm-Trp* transformations undergoes simultaneously and very rapidly. After release the pressure, the *sfm-Trp* units changed to *Trp* units immediately. This result shows that the *sfm-Trp* coordination geometry is very unstable. Fe_{B1} atoms kept its six-fold coordination completely throughout the simulation.

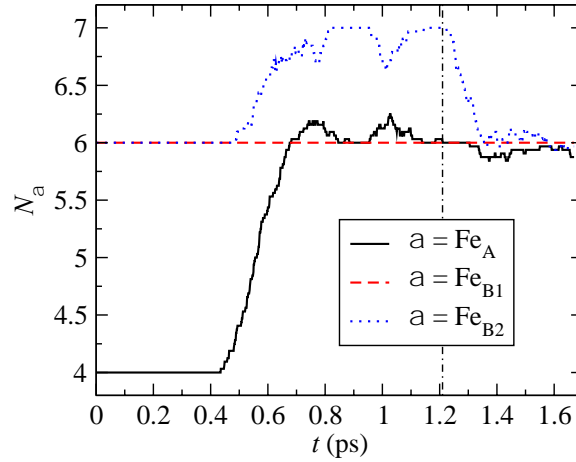


Fig. 5. Average coordination number of the Fe_A (black solid curve), Fe_{B1} (red dashed curve) and Fe_{B2} (blue dotted curve). The bond cutoff distance of 2.55 Å was employed for Fe-O bonds. The black dashed dotted line indicates the final step of the uniaxial strain simulation.

§3. Conclusion

In this study, the structural properties of magnetite under uniaxial compression along the [110] direction were investigated based on the first-principles molecular dynamics simulation. During the simulation, the US phase consisting of *Oct*, *Trp* and *sfm-Trp* centered coordinated Fe atoms and RUS phase consisting of *Oct* and *Trp* centered coordinated Fe atoms were observed in the simulation. In these transformation processes, four-fold coordinated and half of six-fold coordinated Fe atoms changed their coordination geometry. It is expected that those phases exhibit new electronic property because the crystal structures are clearly different from previously reported hydrostatic high-pressure phases. Additionally, this uniaxial strain-induced transformation mechanism would be helpful to understand the Verwey transition mechanism in more detail.

Acknowledgments

This study has been supported by a Grant-in-Aid for Japan Society for the Promotion of Science research fellows (16J05234). The authors acknowledge the Supercomputer Center, Institute for Solid State Physics, University of Tokyo and the Research Institute for Information Technology, Kyushu University for the use of their facilities.

References

- 1) R. Zboril, M. Mashlan and D. Petridis, *Chem. Mater.* **14**, 969 (2002).
- 2) M. E. Fleet, *Acta Cryst. B* **37**, 917 (1981).
- 3) E. J. W. Verwey, P. W. Haayman and F. C. Romeijn, *J. Chem. Phys.* **15**, 181 (1947).
- 4) J. P. Wright, J. P. Attfield, and P. G. Radaelli, *Phys. Rev. B* **66**, 214422 (2002).
- 5) S. de Jong, R. Kukreja, C. Trabant, N. Pontius, C. F. Chang, T. Kachel, M. Beye, F. Sorgenfrei, C. H. Back, B. Bräuer, W. F. Schlotter, J. J. Turner, O. Krupin, M. Doehler, D. Zhu, M. A. Hossain, A. O. Scherz, D. Fausti, F. Novelli, M. Esposito, W. S. Lee, Y. D. Chuang, D. H. Lu, R. G. Moore, M. Yi, M. Trigo, P. Kirchmann, L. Pathey, M. S. Golden, M. Buchholz, P. Metcalf, F. Parmigiani, W. Wurth, A. Föhlisch, C. Schüßler-Langeheine, H. A. Dürr, *Nature Mater.* **12**, 882 (2013).
- 6) Y. Nagasawa, M. Kosaka, S. Katano, N. Mori, S. Todo and T. Uwatoko, *J. Phys. Soc. Jpn.* **76**, Suppl. A, 110 (2007).
- 7) P. E. Blöchl, *Phys. Rev. B* **50**, 17953 (1994).
- 8) J. P. Perdew, K. Burke and M. Ernzerhof, *Phys. Rev. Lett.* **77**, 3865 (1996).
- 9) C. E. Cava, L. S. Roman and C. Persson, *Phys. Rev. A* **31**, 1695 (1985).

- 10) S. Nosé, *Mol.Phys.* **52**, 255 (1984); W. G. Hoover, *Phys. Rev. A* **31**, 1695 (1985).
- 11) M. Tuckerman, B. J. Berne and G. J. Martyna, *J. Chem. Phys.* **97**, 1990 (1992).
- 12) S. Ju, T.-Y. Cai, H.-S. Lu and C.-D. Gong, *J. Am. Chem. Soc.* **134**, 13780 (2012).
- 13) K. Shimamura, M. Misawa, S. Ohmura, F. Shimojo, R. K. Kalia, A. Nakano and P. Vashishta, *Appl. Phys. Lett.* **108**, 071901 (2016).
- 14) J. Noh, O. I. Osman, S. G. Aziz, P. Winget and J. L. Brédas, *Sci. Technol. Adv. Mater.* **15**, 044202 (2014)
- 15) Y. Fei, D. J. Frost, H-K. Mao, C. T. Prewitt and D. Hausermann, *Am. Min.* **84**, 203 (1999).
- 16) C. Haavik, S. Stolen, H. Fjellvag, M. Hanfland and D. Hausermann, *Am. Min.* **85**, 514 (2000).